



# Vertical structure of biomass burning aerosol transported over the southeast Atlantic Ocean

Harshvardhan Harshvardhan<sup>1</sup>, Richard Ferrare<sup>2</sup>, Sharon Burton<sup>2</sup>, Johnathan Hair<sup>2</sup>, Chris Hostetler<sup>2</sup>, David Harper<sup>2</sup>, Anthony Cook<sup>2</sup>, Marta Fenn<sup>3</sup>, Amy Jo Scarino<sup>3</sup>, Eduard Chemyakin<sup>3</sup>, and Detlef Müller<sup>4</sup>

<sup>1</sup>Department of Earth, Atmospheric and Planetary Sciences, Purdue University, West Lafayette, IN, United States

<sup>2</sup>NASA Langley Research Center, Hampton, VA, United States

<sup>3</sup>Science Systems and Applications, Inc./NASA Langley Research Center, Hampton, VA, United States

<sup>4</sup>Department of Physics, Astronomy and Mathematics, University of Hertfordshire, Hatfield, Hertfordshire, United Kingdom

**Correspondence:** Harshvardhan Harshvardhan (harshvar@purdue.edu)

Received: 12 October 2021 – Discussion started: 16 December 2021

Revised: 4 June 2022 – Accepted: 7 July 2022 – Published: 3 August 2022

**Abstract.** Biomass burning in southwestern Africa produces smoke plumes that are transported over the Atlantic Ocean and overlie vast regions of stratocumulus clouds. This aerosol layer contributes to direct and indirect radiative forcing of the atmosphere in this region particularly during the months of August, September, and October. There was a multi-year international campaign to study this aerosol and its interactions with clouds. Here, we report on the evolution of aerosol distributions and properties as measured by the airborne high spectral resolution lidar (HSRL-2) during the ORACLES (Observations of Aerosols above Clouds and their intERactions) campaign in September 2016. The NASA Langley HSRL-2 instrument was flown on the NASA ER-2 aircraft for several days in September 2016. Data were aggregated at two pairs of  $2^\circ \times 2^\circ$  grid boxes to examine the evolution of the vertical profile of aerosol properties during transport over the ocean. Results showed that the structure of the profile of aerosol extinction and microphysical properties is maintained over a 1 to 2 d timescale. In the 3–5 km altitude range, 95 % of the aerosol extinction was contributed by particles in the 0.05–0.50  $\mu\text{m}$  radius size range with the aerosol in this size range having an average effective radius of 0.16  $\mu\text{m}$ . This indicates that there is essentially no scavenging or dry deposition at these altitudes. Moreover, there is very little day-to-day variation in these properties, such that time sampling as happens in such campaigns may be representative of longer periods such as monthly means. Below 3 km, there is considerable mixing with larger aerosol, most likely continental source near land. Furthermore, these measurements indicated that there was often a distinct gap between the bottom of the aerosol layer and cloud tops at the selected locations as evidenced by a layer of several hundred meters that contained relatively low aerosol extinction values above the clouds.

## 1 Introduction

Aerosols are often considered as the most confounding element in the climate system when simulating parameters of the Earth's current climate. Their interaction with clouds makes the problem extremely complicated. The general topic of aerosol–cloud interaction has been of great interest in the scientific community: to quote the report of the Intergovern-

mental Panel on Climate Change (IPCC AR5), “clouds and aerosols continue to contribute the largest uncertainty to estimates and interpretations of the Earth's changing energy budget” (Boucher et al., 2013).

In the context of these interactions, the interplay of biomass burning (BB) aerosol and the stratocumulus clouds in the southeast (SE) Atlantic is unique and crucial to the es-

timates of the energy budget of the region. This BB aerosol arises from the seasonal burning (July–October) of agricultural residue in the southwestern African savanna and traverses large distances westward over the SE Atlantic Ocean. Unlike the aerosol from industrial activity and biofuels that intermingle with clouds in many regions (Ramanathan et al., 2001; Mechoso et al., 2013), these optically thick BB aerosol layers overlay vast stretches of marine stratus cloud in the SE Atlantic (Chand et al., 2009; Wilcox, 2010; Adebisi et al., 2020) where they have a direct radiative effect. The BB aerosol can also act as nuclei for cloud droplets and so cause a potentially significant cloud albedo effect. Observations and modeling studies of such interactions in the south-east Atlantic and southern Africa regions include Diamond et al. (2018), Kacarab et al. (2020), Mallet et al. (2020), and Gupta et al. (2022). There is also some evidence that aerosol can alter the thermodynamics of cloud formation through semi-direct effects (Sakaeda et al., 2011). Studies using high resolution limited area models have shown a variety of effects including stratus to cumulus transition resulting from these interactions (Yamaguchi et al., 2015; Gordon et al., 2018; Lu et al., 2018). The semi-direct effect has also been shown to be important in a limited time run of a global model (Das et al., 2020).

During the course of its transport over the Atlantic basin, the dense BB aerosol layer affects the underlying clouds and Earth's radiative balance in multiple ways. It exerts a direct radiative forcing (DRF) by scattering and absorbing solar radiation in the atmosphere; when clouds are present, these aerosols absorb incoming solar radiation along with the radiation reflected by the underlying cloud surface (Chand et al., 2009; Meyer et al., 2013; Zhang et al., 2016). Simultaneously, depending on the relative vertical location of the aerosol with respect to the cloud deck, the cloud cover (fraction) or liquid water path may increase or decrease in response to heating of surrounding air masses due to aerosol absorption and subsequent changes in atmospheric stability: the semi-direct forcing (Sakaeda et al., 2011; Wilcox, 2012; Das et al., 2020). Observations at Ascension Island show that daytime cloud cover and relative humidity are lower when there is more smoke in the marine boundary layer (Zhang and Zuidema, 2019). Moreover, as the marine boundary layer (MBL) deepens farther offshore and north of 5° S, subsiding aerosol particles become entrained into the MBL and interact with the clouds as cloud condensation nuclei to affect their microphysics (indirect forcing) (Costantino and Bréon, 2013; Painemal et al., 2014).

In the context of simulating the above alluded aerosol radiative effects, it is vital that aerosol–cloud overlap characteristics are accurately represented within the models. The quantification of these aerosol–cloud overlap characteristics in the models is necessary for a variety of reasons. For example, previous studies have found that the sign and magnitude of DRF of absorbing aerosol above clouds (AAC) critically depends upon the reflectance and coverage of the underlying

cloud surfaces along with the optical properties, composition, and size distribution of the overlying aerosols (Keil and Haywood, 2003; Chand et al., 2009). Additionally, the magnitude and sign of the aerosol semi-direct effects are quite sensitive to the vertical distribution of aerosols especially with respect to the vertical location of clouds (Penner et al., 2003; McFarquhar and Wang, 2006; Koch and Del Genio, 2010).

Here, we address the evolution of the vertical properties of BB aerosol as it travels in the marine environment after leaving the African land mass. Section 2 identifies the field campaign and specifies the geographic region selected for the analysis and rationale for that choice. Section 3 describes the attributes of the instrument and key parameters related to the aerosol that can be extracted from the measurements. Section 4 presents the results, followed by a summary and conclusion in Sect. 5.

## 2 Field campaigns

The concerns mentioned above were the driving force behind plans for several international multi-year field campaigns; ORACLES (Observations of Aerosols above Clouds and their interactionS, Redemann et al., 2021), CLARIFY-2017 (CLOUD–Aerosol–Radiation Interactions and Forcing for Year 2017, Haywood et al., 2021), and LASIC (Layered Atlantic Smoke Interactions with Clouds, Zuidema et al., 2016, 2018). A key component of the September 2016 NASA ORACLES Intensive Observation Period (IOP) was the vertical profiling of aerosol properties measured by an airborne lidar, the NASA Langley High Spectral Resolution Lidar-2, HSRL-2 (Burton et al., 2018), on board the NASA ER-2, which was based in Walvis Bay, Namibia for operations during 2016, the deployment covered in this study. In the following 2 years, the instrument was on board the P-3 flying out of São Tomé. The siting and flight tracks chosen ensured adequate coverage of the seasonal BB aerosol.

### 2.1 Meteorology

The September monthly mean meteorological situation is shown in Fig. 1 from Modern-Era Retrospective analysis for Research and Applications, Version 2 (MERRA2) reanalysis (Buchard et al., 2017; Randles et al., 2017) along with locations of relevant sites. A thorough meteorological analysis for all ORACLES deployments is provided in Ryoo et al. (2021). For the period under consideration here, they found that the African Easterly Jet–South (AEJ–S), fast-moving zonal easterlies centered on 650 hPa around 5–15° S, was active and corresponded closely to the long-term climatology. Figure 2 shows 650 hPa winds from MERRA2 reanalysis at the beginning, at the end, and on 2 intermediate days during which HSRL-2 measurements were made. ER-2 flight tracks during the September 2016 IOP are shown in Fig. 3. Note that flights were primarily confined to within roughly

1000 km of the African coast with only the 22 September flight venturing further. Flights such as executed during the IOP are unable to follow air parcels in a Lagrangian fashion to examine the evolution of smoke plumes. Here, we provide an alternate framework by which to study evolving aerosol properties in an average sense. In order to establish average characteristics of the BB smoke plume as it travels over the ocean, we have chosen five grid boxes of  $2^\circ$  latitude and longitude on a side at various distances from the source and aggregated observations. The choice of grid boxes was based on the availability of data from the flights (Fig. 3) and the general direction of transport of the smoke as evidenced by the wind fields in Fig. 2. The grid boxes so chosen are marked on Figs. 2 and 3, and the rationale for the choice is explained below.

Figure 4 shows 48 h backward trajectory frequency analyses at 3.5 km, roughly the central altitude of the plume using NOAA Hybrid Single-Particle Lagrangian Integrated Trajectory (HYSPLIT) trajectory calculations ([https://www.ready.noaa.gov/HYSPLIT\\_traj.php](https://www.ready.noaa.gov/HYSPLIT_traj.php), last access: 18 September 2021) which were carried out using archived Global Data Assimilation System (GDAS)  $0.5^\circ$  meteorology (Stein et al., 2015). The frequency distribution is a 48 h history of the paths taken by air parcels arriving at the grid boxes marked A and C at 3500 m altitude. The time period of the frequency analyses covers the entire period during which HSRL-2 measurements were made, 12–24 September 2016. The selected grid box pairs indicate that Box A receives aerosol that has earlier crossed Box B, and Box C is downwind of Box D; boxes B and D receive aerosol directly from BB sources on land. The grid box pairs A/B and C/D can therefore provide information on the evolution of the microphysics and vertical distribution of BB aerosol plumes after leaving the continent. This strategy is similar to that used in comparisons of models with observations for this campaign by Shinzuka et al. (2020), who also showed that observations made on the sampled days were representative of monthly means. In addition to the four boxes strongly influenced by smoke, a southern box, E, has been chosen to provide a control contrast to the other areas in that it is influenced primarily by maritime air as seen from Figs. 1 and 2.

## 2.2 ORACLES 2016 IOP

The days during the campaign that were included in the averaging procedure are shown in Table 1. Also included is the typical time of the day when the measurements were made, which is a function of the flight pattern of the ER-2. The number of lidar return profiles averaged for each grid box and statistics related to the backward trajectories are also listed. These grid boxes contained aircraft tracks on multiple days during which trajectory analysis showed near-uniform wind direction between 2.5 and 4.5 km altitude throughout the IOP. With the exception of the grid box centered at  $22^\circ$  S,  $9^\circ$  E, all indicate flow from the source region of BB aerosol.

Table 1 also lists the mean and standard deviation of time duration in hours spent over water of air parcels arriving at 3500 m altitude at the grid box during the averaging period. There is no entry for Box E since arriving air had a maritime source and did not originate from land. It must be stressed that the duration is not calculated from the source region on land which is distributed over a large area of central Africa (e.g., Fig. 9 of Redemann et al., 2021) and cannot be uniquely identified with specific observations made over the ocean. The plume has already been airborne over land for several hours (see Fig. 4) and aerosol would have undergone transformations that occur at short timescales (Cappa et al., 2020). The duration was calculated by running HYSPLIT backward trajectories of air parcels arriving every six hours starting at 06:00 UTC on the days of the first flight and ending at 18:00 UTC on the days of the last flight of the averaging period, and is shown in some detail in Fig. 5 which essentially reflects the profile of the prevailing wind speeds. The inference is that BB smoke at 3500 m altitude arrives at A on average about 30 h after passing B and arrives at C 35 h after passing D. The change in selected aerosol properties as measured by the HSRL-2 during this travel in the marine environment provides information on the evolution of the plume during this time period.

## 3 HSRL-2

The NASA Langley Research Center (LaRC) HSRL-2 uses the HSRL technique to independently retrieve aerosol extinction and backscatter (Shiple et al., 1983; Grund and Elooranta, 1991; She et al., 1992) without a priori assumptions on aerosol type or extinction-to-backscatter ratio. By using the HSRL technique, HSRL-2, like its predecessor HSRL-1 (Hair et al., 2008), provides accurate backscatter profiles even in situations where the lidar beam is attenuated by overlying cloud or aerosol as long as it is not completely attenuated. The LaRC HSRL-2 employs the HSRL technique at 355 and 532 nm, and the standard backscatter technique at 1064 nm. It also measures aerosol and cloud depolarization at all three wavelengths. The HSRL-2 provides vertically resolved measurements of the following extensive and intensive aerosol parameters below the aircraft (approximate archival horizontal,  $\Delta x$ , and vertical resolutions,  $\Delta z$ , are listed assuming ER-2 cruise speed).

- *Extensive parameters*.<sup>1</sup> Backscatter coefficient,  $\beta$ , at 355, 532, and 1064 nm ( $\Delta x \sim 2$  km,  $\Delta z \sim 15$  m); extinction coefficient,  $\alpha$ , at 355 and 532 nm ( $\Delta x \sim 12$  km,

<sup>1</sup>By the term *extensive*, we refer to optical parameters, such as extinction, that are influenced by the amount (concentration) and type (size, composition, shape) of aerosol/cloud particles. *Intensive* properties, on the other hand, are those that depend only on the nature of the particles and not on their quantity or concentration but rather depend only on aerosol type (Anderson et al., 2003).

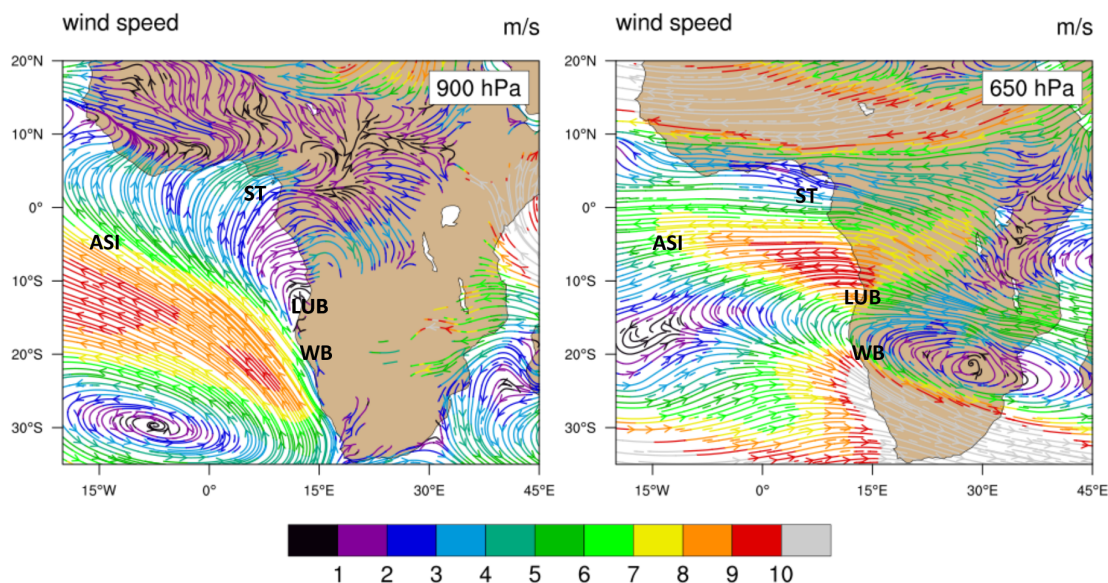


**Figure 1.** MERRA2 monthly mean reanalysis of 900 and 650 hPa streamlines for September 2016. Stations marked are Ascension Island (ASI), Lubango (LUB), a long-term AERONET site at 2 km elevation, and Walvis Bay (WB) where ER-2 flights originated from during the September 2016 ORACLES IOP. Flights in August 2017 and September/October 2018 originated from São Tomé (ST).

**Table 1.** Averaging area, flight time periods, the duration over water and number of HYSPLIT backward trajectories, and number of HSRL-2 profiles in each grid box used in the study.

Box	Averaging area	Averaging days	Time of day	Duration in hours over water at 3.5 km	Number of profiles
A	11–9° S; 1° W–1° E	12 and 16 Sep	11:00 UTC	44.3 ± 7.0 ( $N = 19$ )	50
B	10–8° S; 8–10° E	12, 16, and 18 Sep	10:00 UTC	14.9 ± 4.5 ( $N = 27$ )	56
C	16–14° S; 4–6° E	12 and 16 Sep	13:00 UTC	40.4 ± 7.2 ( $N = 19$ )	51
D	14–12° S; 10–12° E	18 and 24 Sep	09:00 UTC	5.5 ± 2.0 ( $N = 27$ )	46
E	23–21° S; 8–10° E	20 and 22 Sep	14:00 UTC	–	36

$\Delta z \sim 300$  m); and optical depth at 355 and 532 nm (integrating the profile of extinction). The aerosol optical depth (AOD) is a critical quantity in discussions of the influence of aerosol on climate (Boucher et al., 2013).

- *Intensive parameters.* Extinction-to-backscatter ratio of aerosol, the lidar ratio,  $S_a = \alpha_a/\beta_a$ , at 355 and 532 nm ( $\Delta x \sim 12$  km,  $\Delta z \sim 300$  m); depolarization,  $\delta_a = \beta_a^\perp/\beta_a^\parallel$ , at 355, 532, and 1064 nm ( $\Delta x \sim 2$  km,  $\Delta z \sim 15$  m); and aerosol backscatter wavelength dependence (i.e., Ångström exponent for aerosol backscatter – directly related to the backscatter color ratio) for two wavelength pairs (355–532 and 532–1064 nm,  $\Delta x \sim 2$  km,  $\Delta z \sim 15$  m).

The overall systematic error associated with the backscatter calibration is estimated to be less than 5 % for the 355 and 532 nm channels and 20 % for 1064 nm (Burton et al., 2015). Under typical conditions, the total systematic error for extinction is estimated to be less than  $0.01 \text{ km}^{-1}$  at 532 nm. The random errors for all aerosol products are typically less

than 10 % for the backscatter and depolarization ratios (Hair et al., 2008). Rogers et al. (2009) validated the HSRL extinction coefficient profiles and found that the HSRL extinction profiles are within the typical state-of-the-art systematic error at visible wavelengths (Schmid et al., 2006). Since HSRL-2 includes the capability to measure backscatter at three wavelengths and extinction at two wavelengths, “ $3\beta+2\alpha$ ” microphysical retrieval algorithms (Müller et al., 1999a, b; Veselovskii et al., 2002) are used to retrieve height-resolved parameters such as aerosol effective radius and number, surface, and volume concentrations (Müller et al., 2014; Sawamura et al., 2017). Here, we restrict ourselves to the effective radius of the particles.

## 4 Results

In this study of the vertically resolved evolving properties of BB aerosol, we present key lidar measurements and mi-

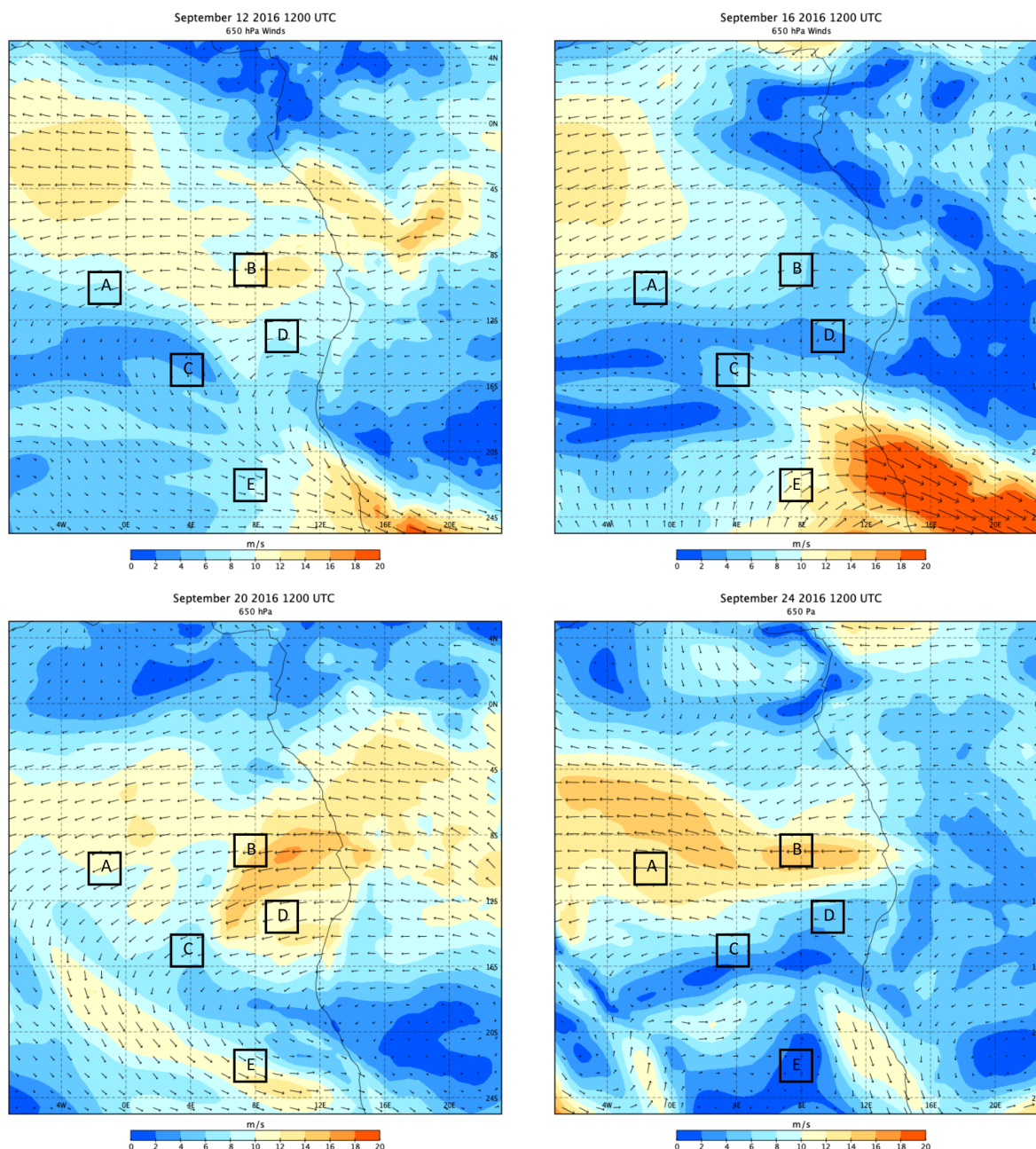


**Figure 2.** MERRA2 reanalysis of 650 hPa winds at 12:00 UTC on 12, 16, 20, and 24 September 2016. Grid boxes in the study are marked with letters.

crophysical results obtained by performing the “ $3\beta+2\alpha$ ” retrieval mentioned in Sect. 3.

#### 4.1 Lidar

Vertical profiles averaged over the times of overflight in  $2^\circ \times 2^\circ$  latitude/longitude boxes shown in Fig. 3 on the days given in Table 1 are for the following properties:

1. Aerosol extinction at 532 nm,  $\alpha_a$ , determined by aerosol number concentration, microphysical properties, and relative humidity;
2. Backscatter Ångström exponent between 1064 and 532 nm, an indication of particle size;
3. Aerosol depolarization at 532 nm, a measure of particle asphericity; and

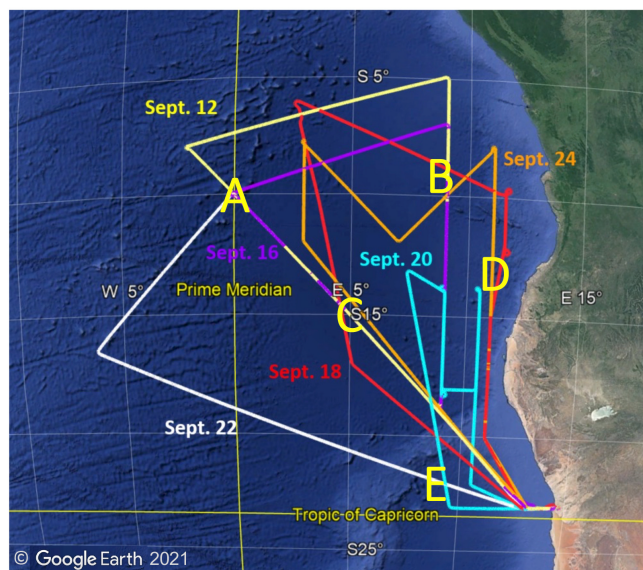


**Figure 3.** HSRL-2 science data flight tracks during the September 2016 IOP. Letters refer to the grid boxes identified in Fig. 2 (© Google Earth).

4. The lidar ratio (ratio of aerosol extinction to backscatter) at 532 nm, a marker for aerosol composition.

Inspection of the wind field at 650 hPa in Fig. 2 and backward trajectory frequency plots in Fig. 4 suggest that the grid boxes chosen fit naturally into two pairs of tracks of the widespread BB aerosol field. The northern pair, identified in Table 1 as A and B, centered around 10° S, is in a faster zonal track whereas the grid boxes C and D are in a track centered between 13–15° S that is slightly slower and has a component from the north over a stretch of water (Fig. 2). The two pairs can then provide information on the evolution of aerosol properties over a time scale of 1 to 2 d. Figures 6–9 show the aerosol extinction, backscatter Ångström exponent, aerosol depolarization, and lidar ratio for the two pairs of grid boxes and Box E which is at the southern edge of the region influenced by the BB aerosol. The results presented are 1 min averages of independent 10 s vertical profiles for backscatter Ångström exponent and depolarization and 1 min averages for extinction and lidar ratio profiles. From Table 1, the mean time elapsed between B and A is 29.4 h and that between D and C is 34.9 h. It should be pointed out that parameter values shown below the level of mean cloud top are averages of lidar returns through breaks in the stratus deck and are not relevant for this study. If we use the low cut-off of an extinction coefficient of  $15 \text{ Mm}^{-1}$  to indicate an aerosol-free layer (Shinozuka et al., 2020), then Fig. 6 indicates that the bulk of the smoke layers encountered at these distances from land were separated from the cloud top, a feature more prevalent during the 2016 IOP than in 2017 and 2018 (Redemann et al., 2021).

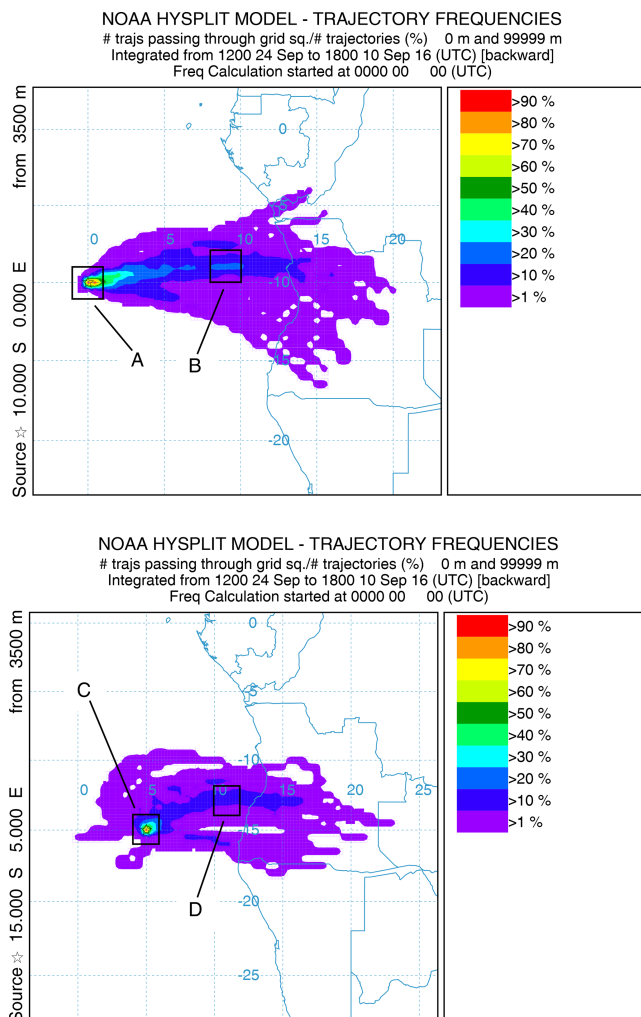


**Figure 4.** Frequency distribution of 48 h backward trajectories of air parcels arriving at 3500 m above the centers of grid boxes A and C over the time period of the campaign. Grid boxes B and D are upstream of grid boxes A and C, respectively.

The northern plume is a column of aerosol of relatively constant extinction from just above 2.5 to 5 km while the southern plume has a profile of extinction that increases nearly linearly with height from a minimum near the cloud top to a maximum at 5 km (Fig. 6). The vertical structure of the aerosol profiles measured by HSRL-2 was compared to water vapor profiles represented by the MERRA2 model. Pistone et al. (2021) explored the relationship between aerosols, CO, and water vapor as measured by ORACLES airborne in situ measurements and represented by models including MERRA2. They found the MERRA2 water vapor profiles, like the measured water vapor profiles, exhibited a linear relationship with CO and biomass burning plume strength; they also found that smoky, humid air produced by daytime convection over the continent advected over the ocean and into the ORACLES study region. MERRA2 water vapor profiles

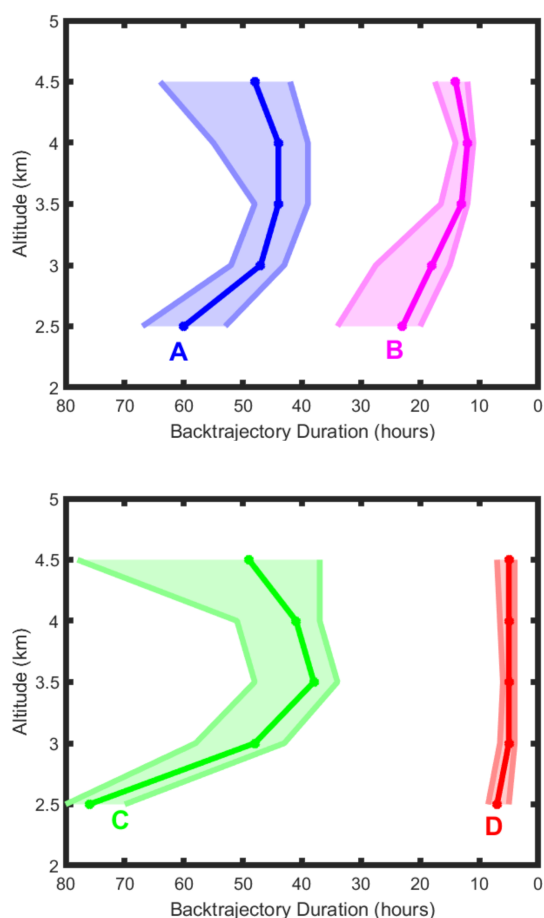


**Figure 5.** Duration of time spent over water of air parcels arriving at grid boxes marked on the figure. Solid lines are median values and the shaded portion is the range of the 75th and 25th percentile. The number of trajectories used for the calculation are in Table 1. Trajectory hours are shown in reverse to correspond to the map in Fig. 4.

produced at 3 h increments and 72 pressure levels were interpolated to the times and locations of the HSRL-2 profiles. Water vapor mixing ratio generally decreased significantly just above the PBL then increased for altitudes around 2 to 3 km before decreasing again. This behavior is generally consistent with the relationship between water vapor and aerosol scattering reported by Pistone et al. (2021).

Figure 10 shows the median, 25th, and 75th percentile relative humidity (RH) profiles computed by interpolating the MERRA2  $0.5^\circ$  3 h humidity profiles to the locations and times of the HSRL-2 measurements. The profiles typically show a more pronounced increase in RH with altitude that more closely follows the HSRL-2 measurements of aerosol extinction profiles, although the MERRA2 profiles typically begin decreasing above 4 km whereas the airborne in situ RH measurements and HSRL-2 aerosol extinction profiles begin decreasing above 5 km. Interestingly, during three of the dates (12, 16, 22 September), considerable portions of

the smoke layers correspond to MERRA2 relative humidity above 60 %–70 %. This increase in RH with altitude could help explain at least some of the increase in aerosol extinction with height observed in the HSRL-2 profiles of the C/D Box pair. Aerosol humidification often amplified the increase in aerosol extinction by factors of 1.5 or more (Doherty et al., 2022).

The Ångström exponent (Fig. 7) and depolarization (Fig. 8) indicate the presence of fine spherical particles at the top of the plume and increasing sizes towards the bottom. The lidar ratio (Fig. 9) above 3 km for the two pairs is between 70 and 80 sr, suggesting strong absorption (Müller et al., 2019), but is considerably less and highly variable in Box E and in the lower layers of the aerosol plume in Box D where the smoke plume most likely has components of continental aerosol such as dust and pollution typical of the nearby Namibian coast (Klopper et al., 2020). The most striking feature of the results is the very small profile-to-profile variability of the intensive lidar parameters in the upper 2 km of the plume over the course of several days as evident from the range of values in the 25–75 percentile shaded grey in Figs. 7–9. This suggests strongly that the particles maintain their size, shape, and absorbing properties over the first few days of transport over the ocean. This result is of some importance for climate studies in which the radiative properties of BB aerosol are input to the calculation of radiative forcing. Complex chain aggregates as found near the source of fires (Pósfai et al., 2003; China et al., 2013) are typically not represented in climate models. However, if the aerosol is already spherical and maintains its size over the time period of radiative interactions being studied, then core–shell models of varying degrees of complexity could perhaps suffice (Zhang et al., 2020). The lower portion of the plume containing larger BB aerosol particles is subject to mixing with marine and continental particles from regions not affected by biomass burning and is highly variable in nature. This would be more difficult to model, but Fig. 6 shows that the aerosol extinction coefficient decreases rapidly at lower levels so errors in representation may be acceptable.

#### 4.2 Microphysics

The lidar measurements are inverted to obtain information regarding particle size. The inversion is performed on 1 min averages of six independent 10 s backscatter profiles and 1 min average extinction profiles. Details of the inversion process are in Müller et al. (2019) and references therein. The particle size distribution is represented using a series of eight triangular basis functions that can represent both monomodal and bimodal size distributions (Müller et al., 2019). Points to note are that the procedure makes the following assumptions: the particles are spherical and homogeneous having wavelength-independent complex index of refraction. The low (< 5 %) values of depolarization through most of the plume, shown in Fig. 8, suggest that the spherical assumption is justified.

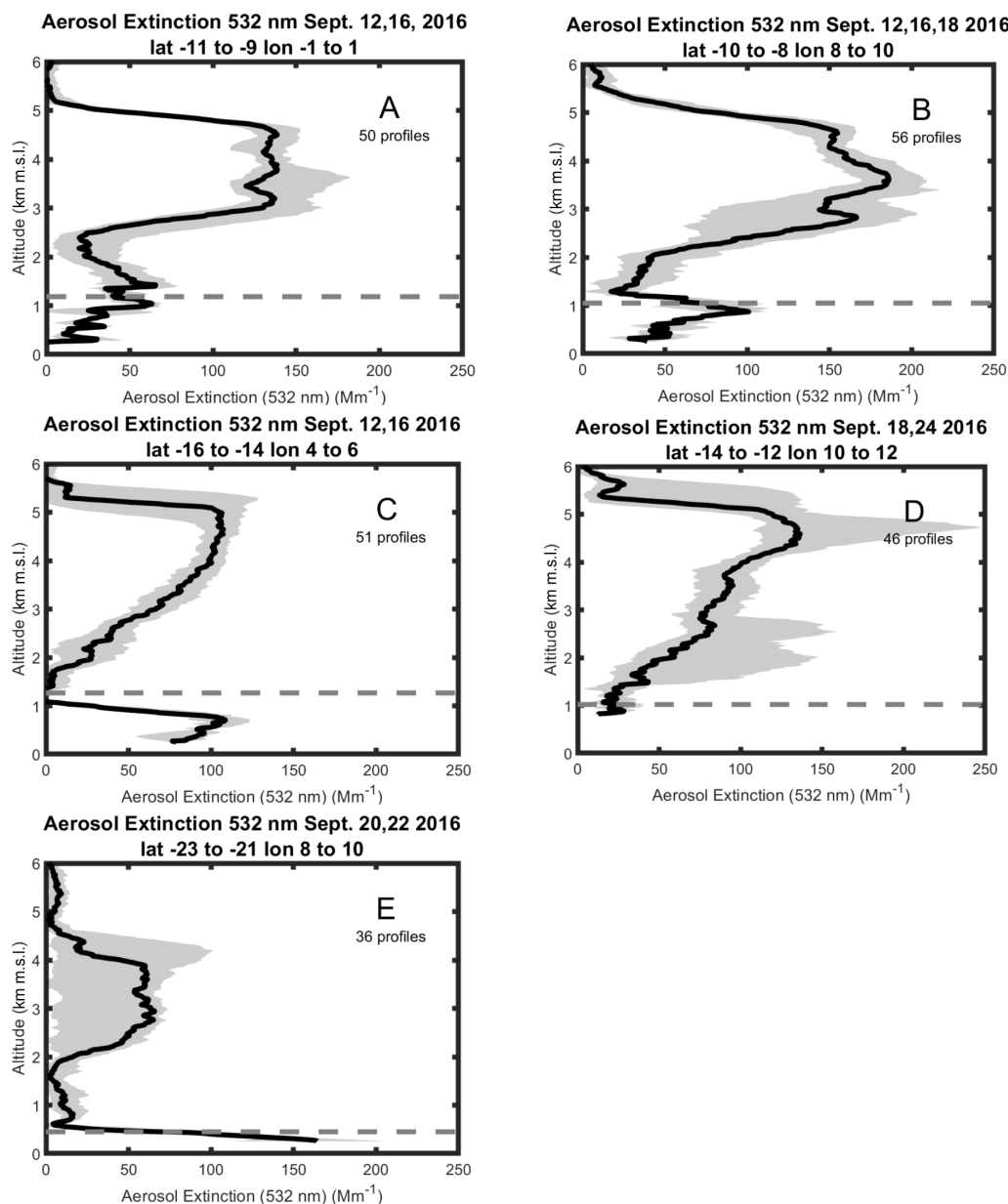


**Figure 6.** Average vertical profiles of the aerosol extinction coefficient at 532 nm in grid boxes A (upper left), B (upper right), C (middle left), D (middle right), and E (lower left). The averaging area, dates of flights, and total number of 1 min profiles are also shown. The dark line represents the median value and gray shades contain the 25th to 75th percentiles. Dashed line refers to the mean cloud top height.

There is most likely structure and inhomogeneity in the core of the particles but current particle optical models are unable to incorporate these complexities. Results from this inversion procedure have been compared to coincident airborne in situ particle measurements. Müller et al. (2014) present results from a campaign off the northeast coast of the US showing that the inversion results agree with in situ measurements of effective radius and also number, surface area, and volume concentration within error bars. Sawamura et al. (2017) report on campaigns in the wintertime San Joaquin Valley of California and summertime near Houston, TX. They found

high correlation and low bias in surface and volume concentration in situ measurements relative to HSRL with the best agreement for submicron fine-mode aerosol which is most relevant to the current study. Müller et al. (2019) report retrievals and their uncertainty for 1 d in the ORACLES campaign, 22 September 2016. Considering only optical data with strong signal-to-noise ratio, they estimate retrieval errors are 25 % for number concentration. The relative uncertainty in effective radius for parts of the flight track where particle size was nearly constant was below 20 %.

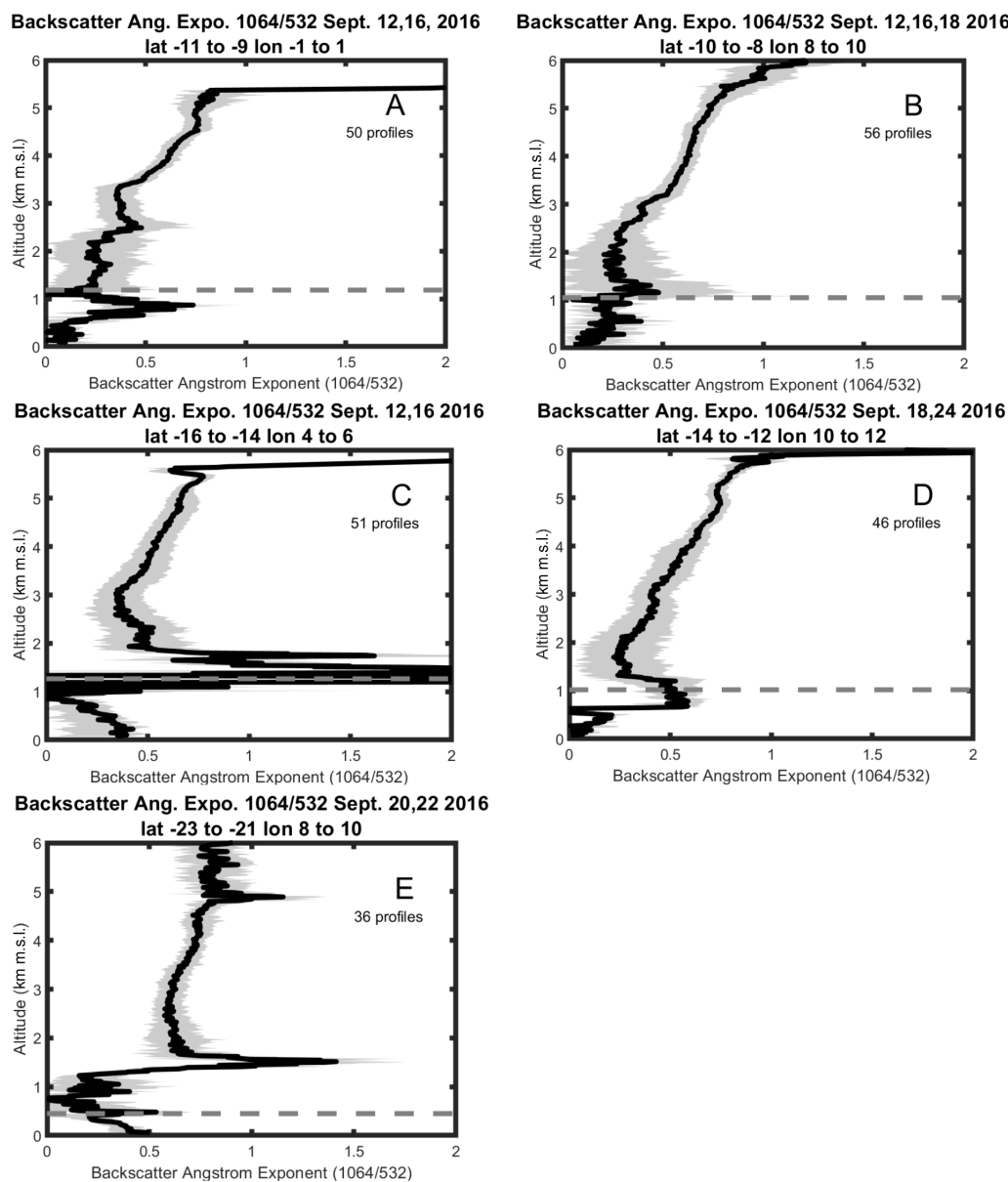


**Figure 7.** As in Fig. 6 but for the wavelength-dependent backscatter Ångström exponent between 1064 and 532 nm.

In order to help separate particles that have BB source from coarser particles of continental or marine origin, we specify a submicron fraction (SMF) as the contribution to the extinction at 532 nm of particles in the radius range 0.05–0.50  $\mu\text{m}$  (Anderson et al., 2005). Figure 11 shows the profiles of SMF for the five grid boxes and, not surprisingly, the bulk of the smoke plume especially between 3 and 5 km contains aerosol almost entirely in the submicron range. Below 3 km, at locations both near and further way from the coast, there is a marked increase in the fraction of larger particles. The increase in depolarization (Fig. 8) at these lower levels and a decrease in the lidar ratio (Fig. 9) suggest mixing with the aforementioned non-BB aerosol particles. However,

the sharp decrease in extinction below 3 km (Fig. 6) indicates that their contribution to direct radiative effects would be minimal. Finally, Fig. 12 shows the vertical profile of the effective radius of the SMF aerosol population. The effective radius is 0.16  $\mu\text{m}$  with little variation between 3 and 5 km. Of greater significance is that it remains very similar between the pairs of grid boxes along the transport trajectory of the smoke. The retrieved effective radius is similar to the results presented by Müller et al. (2014) for a mixture of urban aerosol and smoke. Their comparison with in situ measurements showed a slight overestimate but within a standard deviation. The retrieved and in situ results also show that the particle size is uniform with altitude even when the

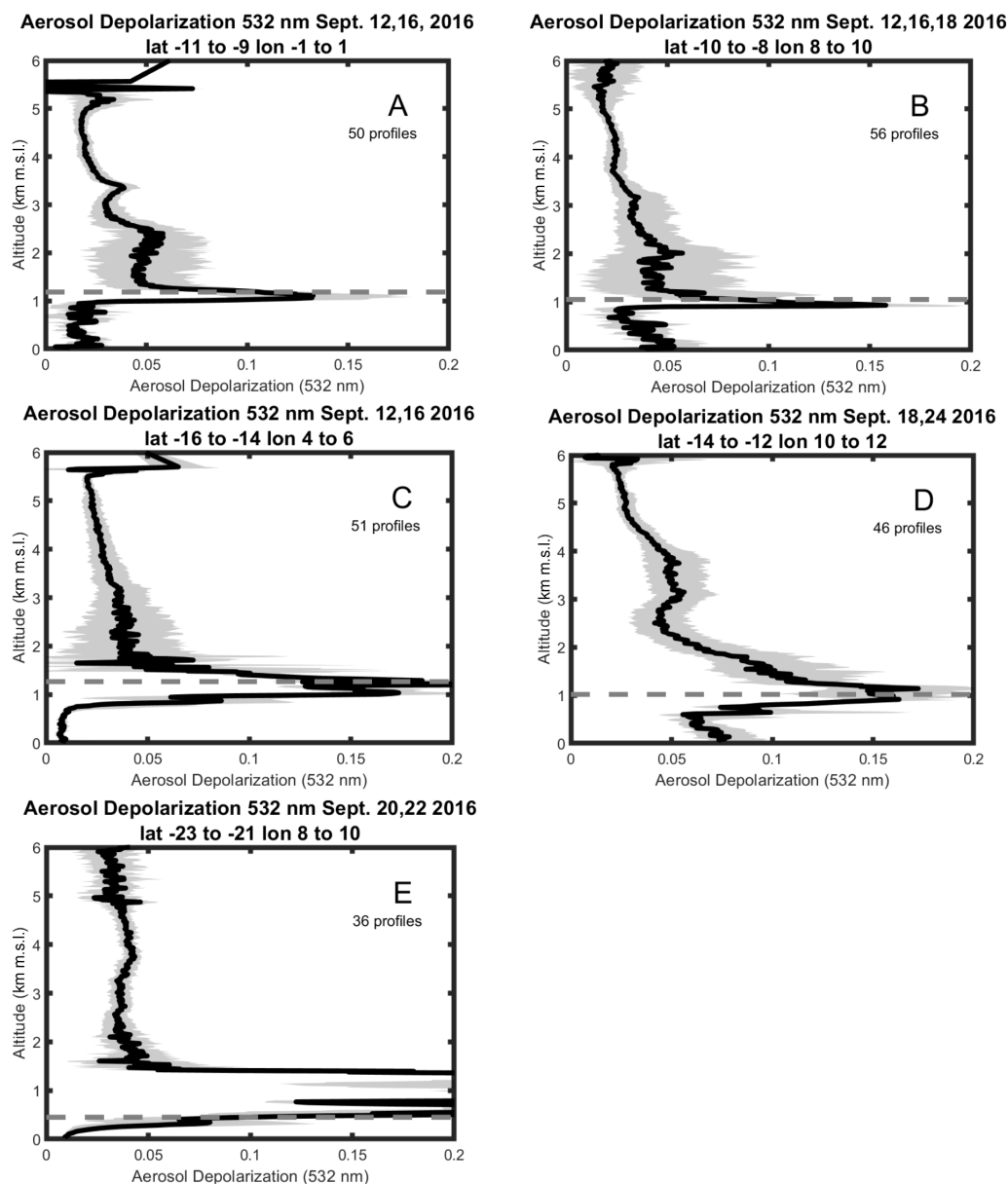


**Figure 8.** As in Fig. 6 but for the aerosol depolarization at 532 nm.

number concentration drops by a factor of 3. Another set of prior comparisons of HSRL-2 and in situ measurements is provided in Sawamura et al. (2017). Here again the effective radius of the submicron fraction of particles,  $0.15\ \mu\text{m}$ , is uniform with altitude and comparable though biased slightly low compared to in situ observations.

The effective radii of the SMF aerosol which typically vary between  $0.15$  to  $0.20\ \mu\text{m}$ , are generally consistent with the sizes reported previously for smoke aerosol in the ORACLES region. Haywood et al. (2021) provide a composite of the aerosol sizes for biomass burning aerosol off the South African coast. These size distributions, which were derived from airborne in situ measurements (Haywood et al.,

2003; Peers et al., 2019; Wu et al., 2020), typically correspond to SMF aerosol effective radii between  $0.14$ – $0.17\ \mu\text{m}$  and were for the dry aerosol. Shinozuka et al. (2020) reported on airborne aerosol sizes measured during ORACLES by an Ultra-High Sensitivity Aerosol Spectrometer (UHSAS) deployed on the NASA P-3 aircraft. The UHSAS measured particles with dry diameters between  $60$  and  $1000\ \text{nm}$ . SMF aerosol effective radii derived from the UHSAS measurements of volume mean diameter were generally around  $0.09$ – $0.10\ \mu\text{m}$  for the dry aerosol. Shinozuka et al. (2020) noted that the UHSAS measurements were somewhat undersized and so were adjusted to account for this effect; this adjustment improved scattering closure with coincident neph-

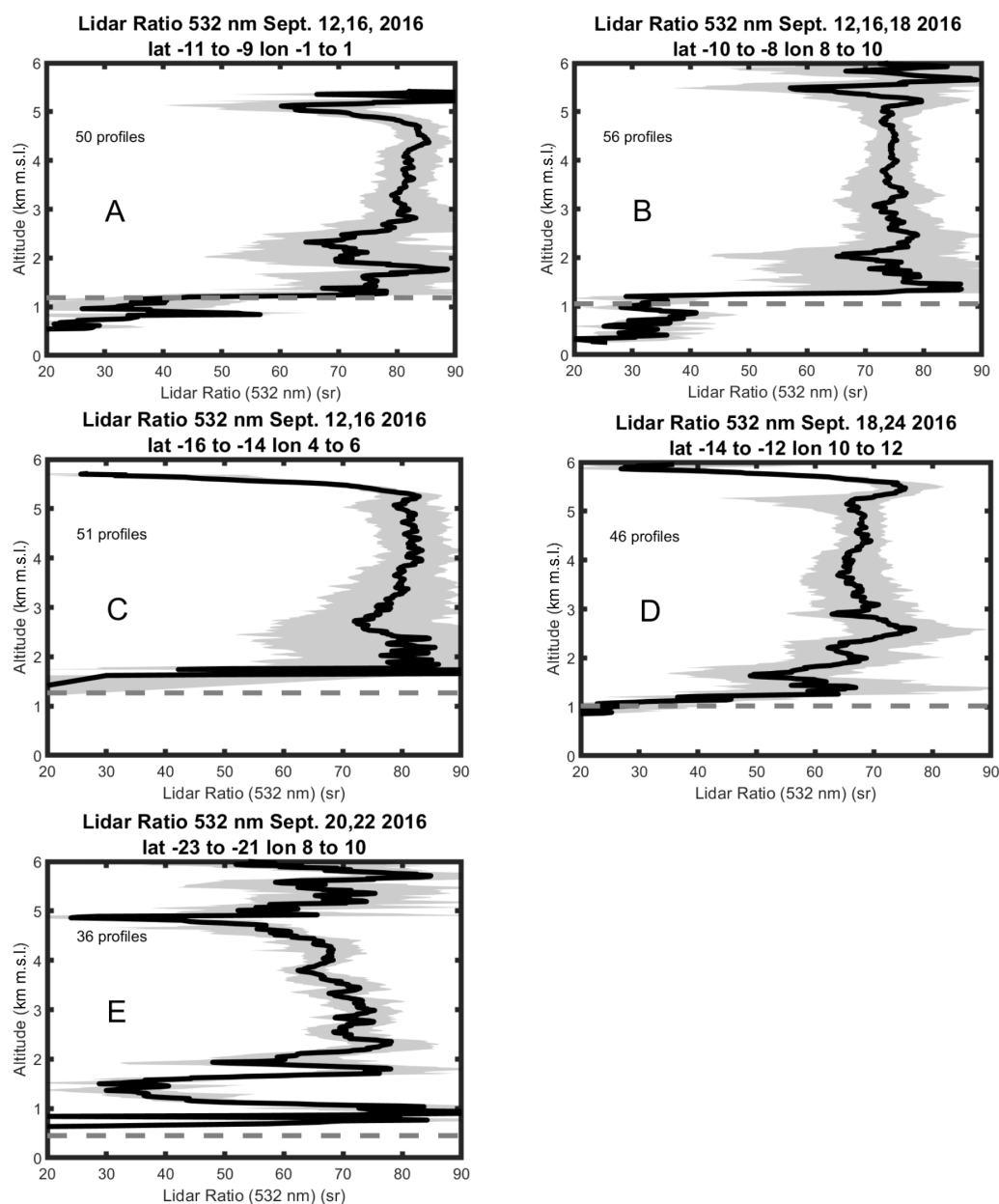


**Figure 9.** As in Fig. 6 but for the lidar ratio at 532 nm.

elometer measurements. As discussed in Sect. 4.1, the RH on some days was above 60 %–70 % so that effective radii under ambient conditions could be expected to be somewhat higher than for the dry aerosol. Using measurements from an airborne Differential Aerosol Sizing and Hygroscopicity Spectrometer Probe (DASH-SP), Shingler et al. (2016) quantified the size-resolved growth factors for several aerosol types; they found that at RH  $\sim$  70 %–80 %, particle diameters for biomass burning aerosols were about 15 %–20 % larger than for the dry aerosol. Xu et al. (2021) derived aerosol properties during the 2016 ORACLES mission using an inversion algorithm that combined HSRL-2 and Re-

search Scanning Polarimeter (RSP) remote sensing measurements. These retrieved aerosol properties were then compared with those derived from the UHSAS measurements described by Shinozuka et al. (2020). For measurements acquired on 12 September 2016, the SMF aerosol effective radius derived from the remote sensing measurements was generally between 0.12–0.15  $\mu\text{m}$  and was only slightly (0.012  $\mu\text{m}$ ) higher than the effective radii for the (dry) SMF aerosol derived from the UHSAS measurements. This suggests that some of this difference is associated with differences in RH between the remote sensing retrievals and the in situ measurements.

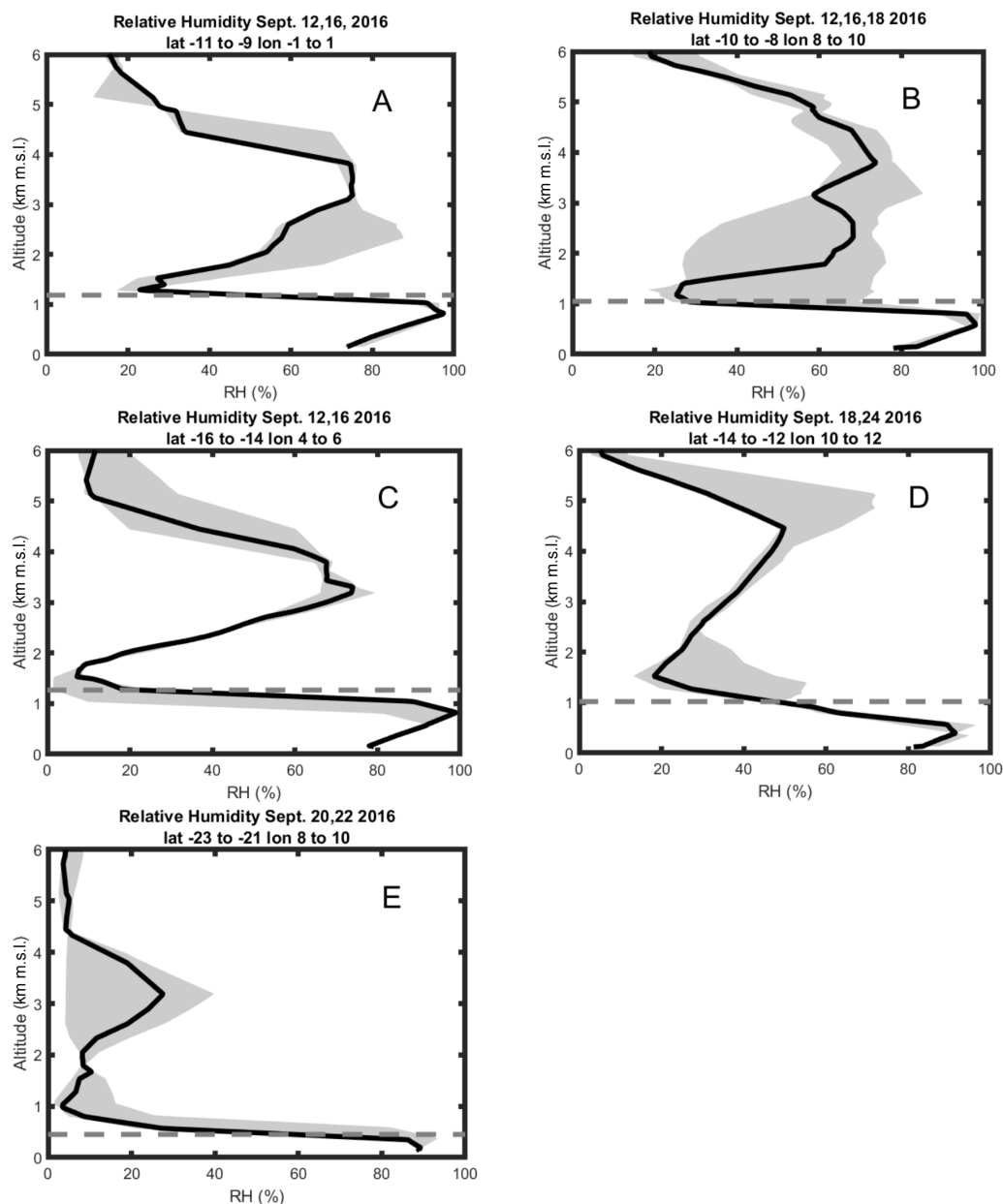


**Figure 10.** Relative humidity (%) in grid boxes A (upper left), B (upper right), C (middle left), D (middle right), and E (lower left) from MERRA2 reanalysis corresponding to the HSRL-2 profiles shown in Figs. 6–9. The dark line represents the median value and gray shades contain the 25th to 75th percentiles. Dashed line refers to the mean cloud top height.

## 5 Conclusions

The results of the aggregated HSRL-2 profiles during the 2016 ORACLES IOP presented here show two main findings. These are however limited to a brief period in the transport of BB smoke from continental Africa over marine clouds in the Atlantic Ocean. This is a limitation of the 2016 campaign because the flight tracks remained within 1000 km of the coast. For the period of 1 to 2 d after crossing the land–ocean boundary, the fraction of all particles that are in the

submicron range in the main smoke plume between 3 and 5 km is around 95%. The effective radius of the submicron particles in this altitude interval is 0.16  $\mu\text{m}$  and essentially constant with altitude. The particle size is comparable to measured particle sizes in previous campaigns that sampled aerosol that was a mixture of urban haze and smoke (Müller et al., 2014; Sawamura et al., 2017). Moreover, the shape of the median vertical profile of extinction does not change during the first 2 d of transport over water suggesting the absence of dry deposition and wet scavenging. The low ( $< 0.05$ ) de-

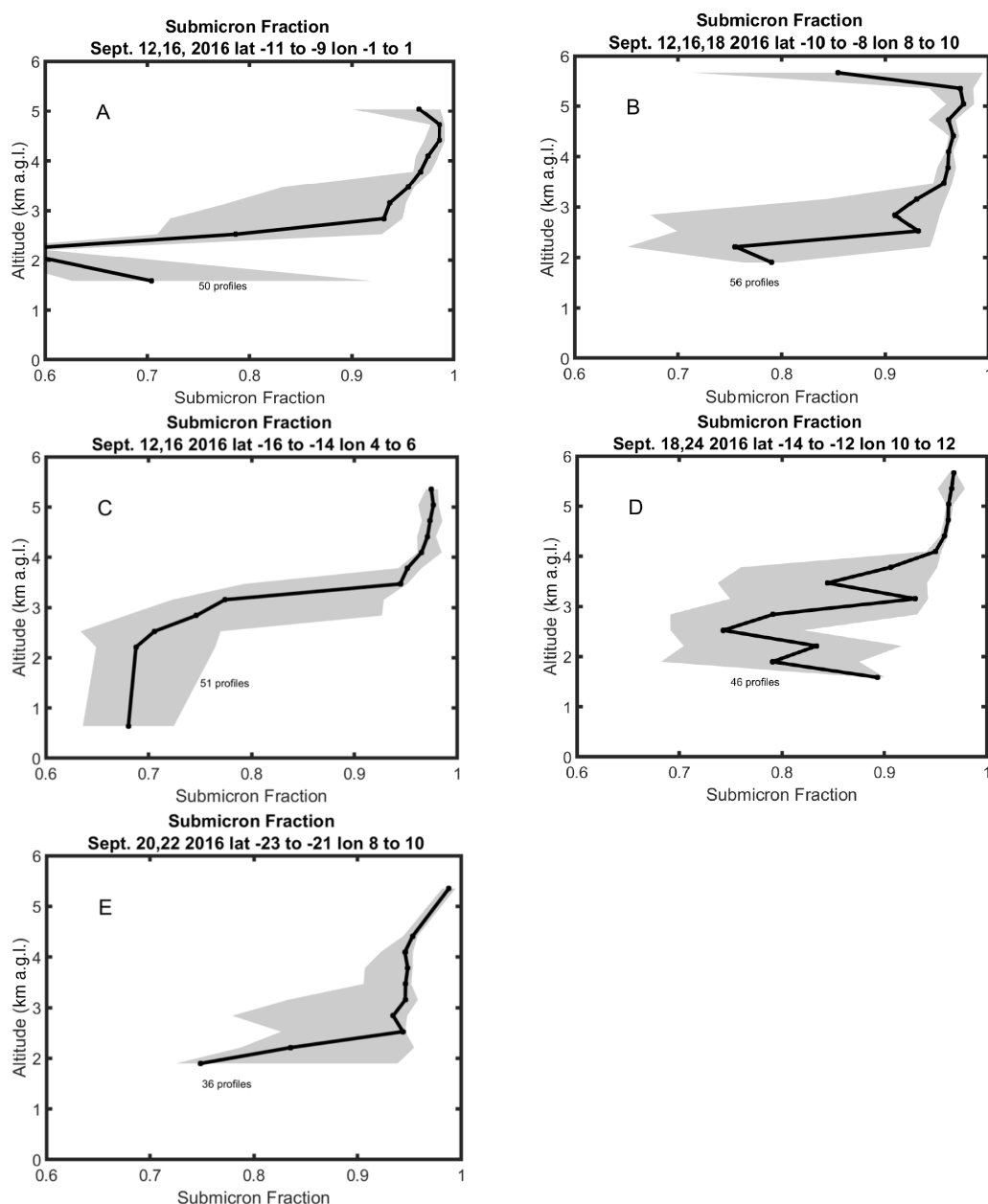


**Figure 11.** Average vertical profiles of the submicron fraction in grid boxes A (upper left), B (upper right), C (middle left), D (middle right), and E (lower left). The averaging area, dates of flights, and total number of 1 min profiles in the average are also shown. The dark line represents the median value and gray shades contain the 25th to 75th percentiles.

polarization ratio of the submicron particles signifies that they are well coated and the assumption of sphericity in the inversion procedure and models that estimate the radiative effects of aerosol is justified. The BB aerosol mixed with continental and marine aerosol at the base of the plume but during the September 2016 IOP this layer of mixed aerosol tended to have very low extinction coefficients suggesting low abundance, and there was often a distinct gap between the plume and the cloud tops.

The HSRL-2 instrument was also deployed in the 2017 and 2018 ORACLES campaigns but was deployed on the NASA P-3 which often flew at low altitude to acquire in situ measurements of aerosols and clouds. Consequently, the HSRL-2 was not able to make continuous measurements of the BB aerosol plumes in a manner similar as when deployed on the ER-2. However, there are segments of the track that can provide similar information to the data obtained in the 2016 campaign but for a different time period. Moreover, some flight tracks extended much further from land (Doherty

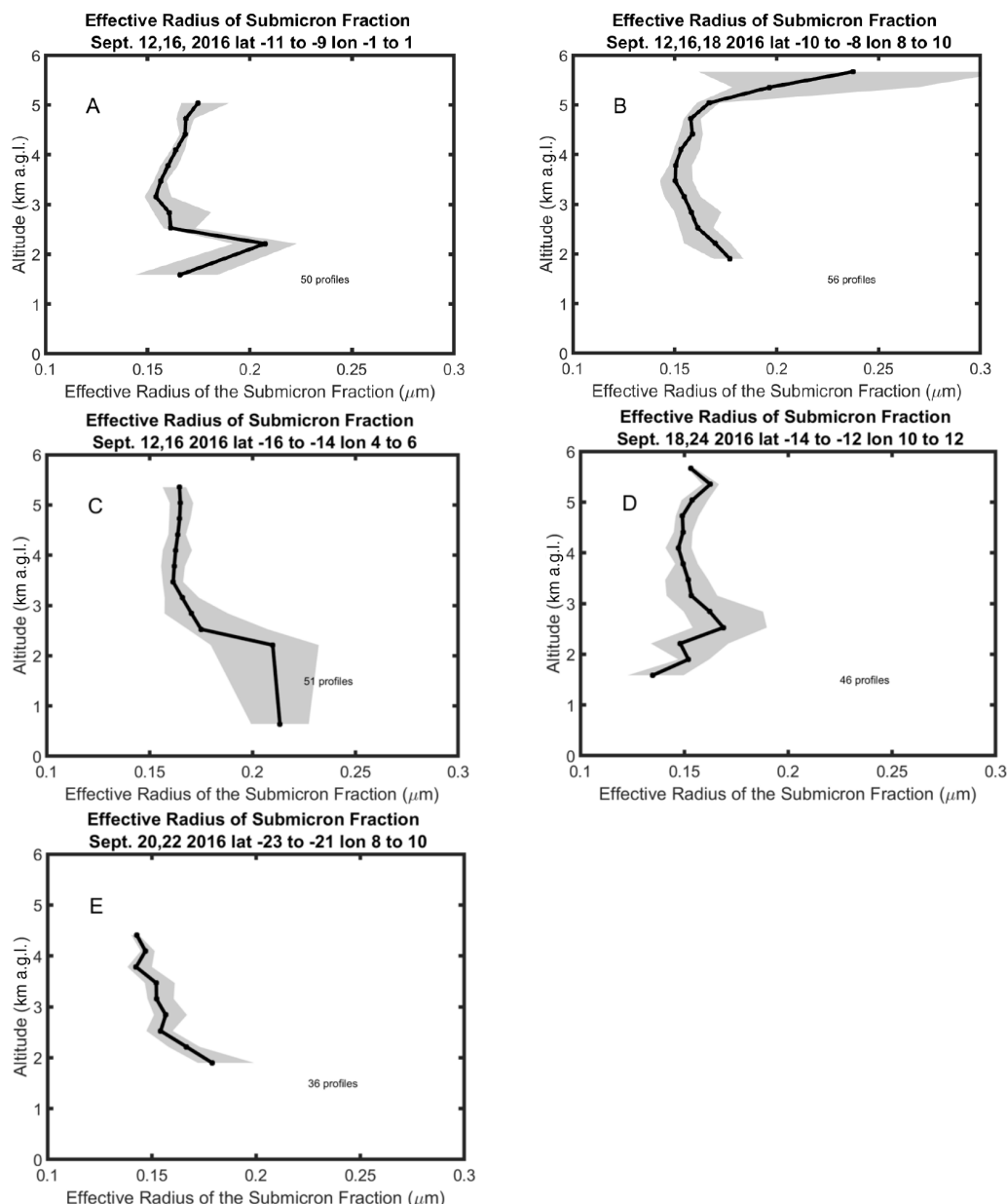


**Figure 12.** As in Fig. 11 but for the effective radius of the submicron fraction.

et al., 2022). Analysis of the later campaigns will provide information on the physical evolution of aerosol that has aged for a longer period than is covered in this study.

**Data availability.** HSRL-2 optical data and retrieved inversion data are available at the NASA archive site <https://espoarchive.nasa.gov/archive/browse/oracles/id8/ER2> (last access: 22 April 2017) and all ORACLES data are accessible via the digital object identifier (DOI) provided under ORACLES Science Team (2020) reference [https://doi.org/10.5067/Suborbital/ORACLES/ER2/2016\\_V2](https://doi.org/10.5067/Suborbital/ORACLES/ER2/2016_V2).

**Author contributions.** HH performed smoke backward trajectories and analyses related to HSRL-2 products and wrote most of the paper. JH, CH, DH, AC developed the instrument. DH, AC operated the instrument. RF, SB developed plans for deploying the instrument and performed analyses of HSRL-2 data products. RF produced sections of the paper and produced HSRL-2 graphics. MF, AJS produced HSRL-2 data products. EC and DM developed and implemented multiwavelength lidar retrievals.

**Competing interests.** The contact author has declared that none of the authors has any competing interests.

**Disclaimer.** Publisher's note: Copernicus Publications remains neutral with regard to jurisdictional claims in published maps and institutional affiliations.

**Acknowledgements.** The lead author would like to thank NASA Langley Research Center for hosting him during a sabbatical when this study was initiated. We wish to thank the NASA ER-2 pilots and ground crew for their extensive support during ORACLES. The authors gratefully acknowledge the NOAA Air Resources Laboratory (ARL) for the provision of the HYSPLIT transport and dispersion model and READY website (<https://www.ready.noaa.gov>, last access: 18 September 2021) used in this publication.

**Financial support.** HSRL-2 participation in ORACLES was supported by NASA through the Earth Venture Suborbital-2 (EVS-2) program (grant no. 13-EVS2-13-0028). Funding for this work was also provided by NASA through the Radiation Sciences Program.

**Review statement.** This paper was edited by Nikos Hatzianastassiou and reviewed by two anonymous referees.

## References

- Adebiyi, A. A., Zuidema, P., Chang, I., Burton, S. P., and Cairns, B.: Mid-level clouds are frequent above the southeast Atlantic stratocumulus clouds, *Atmos. Chem. Phys.*, 20, 11025–11043, <https://doi.org/10.5194/acp-20-11025-2020>, 2020.
- Anderson, T. L., Charlson, R. J., Winker, D. M., Ogren, J. A., and Holmén, K.: Mesoscale variations of tropospheric aerosols, *J. Atmos. Sci.*, 60, 119–136, 2003.
- Anderson, T. L., Wu, Y., Chu, D. A., Schmid, B., Redemann, J., and Dubovik, O.: Testing the MODIS satellite retrieval of aerosol fine-mode fraction, *J. Geophys. Res.*, 110, D18204, <https://doi.org/10.1029/2005JD005978>, 2005.
- Boucher, O., Randall, D., Artaxo, P., Bretherton, C., Feingold, G., Forster, P., Kerminen, V.-M., Kondo, Y., Liao, H., Lohmann, U., Rasch, P., Satheesh, S. K., Sherwood, S., Stevens, B., and Zhang, X. Y.: Clouds and Aerosols, in: *Climate Change 2013: The Physical Science Basis. Contribution of Working Group I to the Fifth Assessment Report of the Intergovernmental Panel on Climate Change*, edited by: Stocker, T. F., Qin, D., Plattner, G.-K., Tignor, M., Allen, S. K., Boschung, J., Nauels, A., Xia, Y., Bex, V., and Midgley, P. M., Cambridge University Press, 571–657, <https://doi.org/10.1017/CBO9781107415324.016>, 2013.
- Buchard, V., Randles, C. A., da Silva, A. M., Darmenov, A., Colarco, P. R., Govindaraju, R., Ferrare, R. A., Hair, J., Beyersdorf, A. J., Ziemba, L. D., and Yu, H.: The MERRA-2 aerosol reanalysis, 1980 onwards Part II: Evaluation and case studies, *J. Climate*, 30, 6851–6871, <https://doi.org/10.1175/JCLI-D-16-0613.1>, 2017.
- Burton, S. P., Hair, J. W., Kahnert, M., Ferrare, R. A., Hostetler, C. A., Cook, A. L., Harper, D. B., Berkoff, T. A., Seaman, S. T., Collins, J. E., Fenn, M. A., and Rogers, R. R.: Observations of the spectral dependence of linear particle depolarization ratio of aerosols using NASA Langley airborne High Spectral Resolution Lidar, *Atmos. Chem. Phys.*, 15, 13453–13473, <https://doi.org/10.5194/acp-15-13453-2015>, 2015.
- Burton, S. P., Hostetler, C. A., Cook, A. L., Hair, J. W., Seaman, S., Scola, S., Harper, D. B., Smith, J. A., Fenn, M. A., Ferrare, R. A., Saide, P. E., Chemyakin, E. V., and Müller, D.: Calibration of a high spectral resolution lidar using a Michelson interferometer with data examples from ORACLES, *Appl. Optics*, 57, 6061–6075, 2018.
- Cappa, C. D., Lim, C. Y., Hagan, D. H., Coggon, M., Koss, A., Sekimoto, K., de Gouw, J., Onasch, T. B., Warneke, C., and Kroll, J. H.: Biomass-burning-derived particles from a wide variety of fuels – Part 2: Effects of photochemical aging on particle optical and chemical properties, *Atmos. Chem. Phys.*, 20, 8511–8532, <https://doi.org/10.5194/acp-20-8511-2020>, 2020.
- Chand, D., Wood, R., Anderson, T. L., Satheesh, S. K., and Charlson, R. J.: Satellite-derived direct radiative effect of aerosols dependent on cloud cover, *Nat. Geosci.*, 2, 181–184, <https://doi.org/10.1038/Ngeo437>, 2009.
- China, S., Mazzoleni, C., Gorkowski, K., Aiken, A. C., and Dubey, M. K.: Morphology and mixing state of individual freshly emitted wildfire carbonaceous particles, *Nat. Commun.*, 4, 2122 <https://doi.org/10.1038/ncomms3122>, 2013.
- Costantino, L. and Bréon, F.-M.: Aerosol indirect effect on warm clouds over South-East Atlantic, from co-located MODIS and CALIPSO observations, *Atmos. Chem. Phys.*, 13, 69–88, <https://doi.org/10.5194/acp-13-69-2013>, 2013.
- Das, S., Harshvardhan, H., and Colarco, P. R.: The influence of elevated smoke layers on stratocumulus clouds over the SE Atlantic in the NASA Goddard Earth Observing System (GEOS) Model, *J. Geophys. Res.-Atmos.*, 125, e2019JD031209, <https://doi.org/10.1029/2019JD031209>, 2020.
- Diamond, M. S., Dobracki, A., Freitag, S., Small Griswold, J. D., Heikkilä, A., Howell, S. G., Kacarab, M. E., Podolske, J. R., Saide, P. E., and Wood, R.: Time-dependent entrainment of smoke presents an observational challenge for assessing aerosol–cloud interactions over the southeast Atlantic Ocean, *Atmos. Chem. Phys.*, 18, 14623–14636, <https://doi.org/10.5194/acp-18-14623-2018>, 2018.
- Doherty, S. J., Saide, P. E., Zuidema, P., Shinozuka, Y., Ferrada, G. A., Gordon, H., Mallet, M., Meyer, K., Painemal, D., Howell, S. G., Freitag, S., Dobracki, A., Podolske, J. R., Burton, S. P., Ferrare, R. A., Howes, C., Nabat, P., Carmichael, G. R., da Silva, A., Pistone, K., Chang, I., Gao, L., Wood, R., and Redemann, J.: Modeled and observed properties related to the direct aerosol radiative effect of biomass burning aerosol over the southeastern Atlantic, *Atmos. Chem. Phys.*, 22, 1–46, <https://doi.org/10.5194/acp-22-1-2022>, 2022.
- Gordon, H., Field, P. R., Abel, S. J., Dalvi, M., Grosvenor, D. P., Hill, A. A., Johnson, B. T., Miltenberger, A. K., Yoshioka, M., and Carslaw, K. S.: Large simulated radiative effects of smoke in the south-east Atlantic, *Atmos. Chem. Phys.*, 18, 15261–15289, <https://doi.org/10.5194/acp-18-15261-2018>, 2018.
- Grund, C. J., and Eloranta, E. W.: University of Wisconsin high spectral resolution lidar, *Opt. Eng.*, 30, 6–12, 1991.
- Gupta, S., McFarquhar, G. M., O'Brien, J. R., Poellot, M. R., Delene, D. J., Miller, R. M., and Small Griswold, J. D.: Factors affecting precipitation formation and precipitation susceptibility of marine stratocumulus with variable above- and below-cloud aerosol concentrations over the Southeast Atlantic, *At-*

- mos. Chem. Phys., 22, 2769–2793, <https://doi.org/10.5194/acp-22-2769-2022>, 2022.
- Hair, J. W., Hostetler, C. A., Cook, A. L., Harper, D. B., Ferrare, R. A., Mack, T. L., Welch, W., Izquierdo, L. R., Hovis, F. E.: Airborne High Spectral Resolution Lidar for profiling aerosol optical properties, *Appl. Optics*, 47, 6734–6752, <https://doi.org/10.1364/AO.47.006734>, 2008.
- Haywood, J. M., Osborne, S. R., Francis, P. N., Keil, A., Formenti, P., Andreae, M. O., and Kaye, P. H.: The mean physical and optical properties of regional haze dominated by biomass burning aerosol measured from the C-130 aircraft during SAFARI 2000, *J. Geophys. Res.*, 108, 8473, <https://doi.org/10.1029/2002JD002226>, 2003.
- Haywood, J. M., Abel, S. J., Barrett, P. A., Bellouin, N., Blyth, A., Bower, K. N., Brooks, M., Carslaw, K., Che, H., Coe, H., Cotterell, M. I., Crawford, I., Cui, Z., Davies, N., Dingley, B., Field, P., Formenti, P., Gordon, H., de Graaf, M., Herbert, R., Johnson, B., Jones, A. C., Langridge, J. M., Malavelle, F., Partridge, D. G., Peers, F., Redemann, J., Stier, P., Szpek, K., Taylor, J. W., Watson-Parris, D., Wood, R., Wu, H., and Zuidema, P.: The CLoud–Aerosol–Radiation Interaction and Forcing: Year 2017 (CLARIFY-2017) measurement campaign, *Atmos. Chem. Phys.*, 21, 1049–1084, <https://doi.org/10.5194/acp-21-1049-2021>, 2021.
- Kacarab, M., Thornhill, K. L., Dobracki, A., Howell, S. G., O'Brien, J. R., Freitag, S., Poellot, M. R., Wood, R., Zuidema, P., Redemann, J., and Nenes, A.: Biomass burning aerosol as a modulator of the droplet number in the southeast Atlantic region, *Atmos. Chem. Phys.*, 20, 3029–3040, <https://doi.org/10.5194/acp-20-3029-2020>, 2020.
- Keil, A. and Haywood, J. M.: Solar radiative forcing by biomass burning aerosol particles during SAFARI 2000: A case study based on measured aerosol and cloud properties, *J. Geophys. Res.-Atmos.*, 108, 8467, <https://doi.org/10.1029/2002JD002315>, 2003.
- Klopper, D., Formenti, P., Namwoonde, A., Cazaunau, M., Chevallier, S., Feron, A., Gaimoz, C., Hease, P., Lahmidi, F., Mirandebret, C., Triquet, S., Zeng, Z., and Piketh, S. J.: Chemical composition and source apportionment of atmospheric aerosols on the Namibian coast, *Atmos. Chem. Phys.*, 20, 15811–15833, <https://doi.org/10.5194/acp-20-15811-2020>, 2020.
- Koch, D. and Del Genio, A. D.: Black carbon semi-direct effects on cloud cover: review and synthesis, *Atmos. Chem. Phys.*, 10, 7685–7696, <https://doi.org/10.5194/acp-10-7685-2010>, 2010.
- Lu, Z., Liu, X., Zhang, Z., Zhao, C., Meyer, K., Rajapakshe, C., Wu, C., Yang, Z., and Penner, J.: Biomass smoke from southern Africa can significantly enhance the brightness of stratocumulus over the southeastern Atlantic Ocean, *P. Natl. Acad. Sci. USA*, 115, 2924–2929, <https://doi.org/10.1073/pnas.1713703115>, 2018.
- Mallet, M., Solmon, F., Nabat, P., Elguindi, N., Waquet, F., Bouniol, D., Sayer, A. M., Meyer, K., Roehrig, R., Michou, M., Zuidema, P., Flamant, C., Redemann, J., and Formenti, P.: Direct and semi-direct radiative forcing of biomass-burning aerosols over the southeast Atlantic (SEA) and its sensitivity to absorbing properties: a regional climate modeling study, *Atmos. Chem. Phys.*, 20, 13191–13216, <https://doi.org/10.5194/acp-20-13191-2020>, 2020.
- McFarquhar, G. M. and Wang, H.: Effects of aerosols on trade wind cumuli over the Indian Ocean: Model simulations, *Q. J. Roy. Meteor. Soc.*, 132, 821–843, <https://doi.org/10.1256/qj.04.179>, 2006.
- Mechoso, C. R., Wood, R., Weller, R., Bretherton, C. S., Clarke, A. D., Coe, H., Fairall, C., Farrar, J. T., Feingold, G., Garreaud, R., Grados, C., McWilliams, J., de Szoeke, S. P., Yuter, S. E., and Zuidema, Z.: Ocean–cloud–atmosphere–land interactions in the Southeastern Pacific: The VOCALS program, *B. Am. Meteorol. Soc.*, 95, 357–375, <https://doi.org/10.1175/BAMS-D-11-00246.1>, 2013.
- Meyer, K., Platnick, S., Oreopoulos, L., and Lee, D.: Estimating the direct radiative effect of absorbing aerosols overlying marine boundary layer clouds in the southeast Atlantic using MODIS and CALIOP, *J. Geophys. Res.-Atmos.*, 118, 4801–4815, <https://doi.org/10.1002/jgrd.50449>, 2013.
- Müller, D., Wandinger, U., and Ansmann, A.: Microphysical particle parameters from extinction and backscatter lidar data by inversion with regularization: theory, *Appl. Optics*, 38, 2346–2357, 1999a.
- Müller, D., Wandinger, U., and Ansmann, A.: Microphysical particle parameters from extinction and backscatter lidar data by inversion with regularization: simulation, *Appl. Optics*, 38, 2358–2368, 1999b.
- Müller, D., Hostetler, C. A., Ferrare, R. A., Burton, S. P., Chemyakin, E., Kolgotin, A., Hair, J. W., Cook, A. L., Harper, D. B., Rogers, R. R., Hare, R. W., Cleckner, C. S., Obland, M. D., Tomlinson, J., Berg, L. K., and Schmid, B.: Airborne Multiwavelength High Spectral Resolution Lidar (HSRL-2) observations during TCAP 2012: vertical profiles of optical and microphysical properties of a smoke/urban haze plume over the northeastern coast of the US, *Atmos. Meas. Tech.*, 7, 3487–3496, <https://doi.org/10.5194/amt-7-3487-2014>, 2014.
- Müller, D., Chemyakin, E., Kolgotin, A., Ferrare, R. A., Hostetler, C. A., and Romanov, A.: Automated, unsupervised, inversion of multiwavelength lidar data with TiARA: assessment of retrieval performance of microphysical parameters using simulated data, *Appl. Optics*, 58, 4981–5007, <https://doi.org/10.1364/AO.58.004981>, 2019.
- ORACLES Science Team: Suite of Aerosol, Cloud, and Radiation Data Acquired Aboard ER2 During ORACLES 2016, Version 2, NASA Ames Earth Science Project Office [data set], [https://doi.org/10.5067/Suborbital/ORACLES/ER2/2016\\_V2](https://doi.org/10.5067/Suborbital/ORACLES/ER2/2016_V2), 2020.
- Painemal, D., Kato, S., and Minnis, P.: Boundary layer regulation in the southeast Atlantic cloud microphysics during the biomass burning season as seen by the A-train satellite constellation, *J. Geophys. Res.-Atmos.*, 119, 11288–11302, <https://doi.org/10.1002/2014JD022182>, 2014.
- Peers, F., Francis, P., Fox, C., Abel, S. J., Szpek, K., Cotterell, M. I., Davies, N. W., Langridge, J. M., Meyer, K. G., Platnick, S. E., and Haywood, J. M.: Observation of absorbing aerosols above clouds over the south-east Atlantic Ocean from the geostationary satellite SEVIRI – Part I: Method description and sensitivity, *Atmos. Chem. Phys.*, 19, 9595–9611, <https://doi.org/10.5194/acp-19-9595-2019>, 2019.
- Penner, J. E., Zhang, S. Y., and Chuang, C. C.: Soot and smoke aerosol may not warm climate, *J. Geophys. Res.-Atmos.*, 108, 4657, <https://doi.org/10.1029/2003JD003409>, 2003.

- Pistone, K., Zuidema, P., Wood, R., Diamond, M., da Silva, A. M., Ferrada, G., Saide, P. E., Ueyama, R., Ryoo, J.-M., Pfister, L., Podolske, J., Noone, D., Bennett, R., Stith, E., Carmichael, G., Redemann, J., Flynn, C., LeBlanc, S., Segal-Rozenhaimer, M., and Shinozuka, Y.: Exploring the elevated water vapor signal associated with the free tropospheric biomass burning plume over the southeast Atlantic Ocean, *Atmos. Chem. Phys.*, 21, 9643–9668, <https://doi.org/10.5194/acp-21-9643-2021>, 2021.
- Pósfai, M., Simonics, R., Li, J., Hobbs, P. V., and Buseck, P. R.: Individual aerosol particles from biomass burning in southern Africa: 1. Compositions and size distributions of carbonaceous particles, *J. Geophys. Res.*, 108, 8483, <https://doi.org/10.1029/2002JD002291>, 2003.
- Ramanathan, V., Crutzen, P. J., Kiehl, J. T., and Rosenfeld, D.: Aerosols, climate, and the hydrological cycle, *Science*, 294, 2119–2124, <https://doi.org/10.1126/science.1064034>, 2001.
- Randles, C. A., daSilva, A. M., Buchard, V., Colarco, P. R., Darmenov, A., Govindaraju, P., Smirnov, A., Holben, B., Ferrare, R. A., Hair, J., Shinozuka, Y., and Flynn, C. J.: The MERRA-2 aerosol reanalysis, 1980 onward. Part I: System description and data assimilation evaluation, *J. Climate*, 30, 6823–6850, <https://doi.org/10.1175/JCLI-D-16-0609.1>, 2017.
- Redemann, J., Wood, R., Zuidema, P., Doherty, S. J., Luna, B., LeBlanc, S. E., Diamond, M. S., Shinozuka, Y., Chang, I. Y., Ueyama, R., Pfister, L., Ryoo, J.-M., Dobracki, A. N., da Silva, A. M., Longo, K. M., Kacenelenbogen, M. S., Flynn, C. J., Pistone, K., Knox, N. M., Piketh, S. J., Haywood, J. M., Formenti, P., Mallet, M., Stier, P., Ackerman, A. S., Bauer, S. E., Fridlind, A. M., Carmichael, G. R., Saide, P. E., Ferrada, G. A., Howell, S. G., Freitag, S., Cairns, B., Holben, B. N., Knobelspiese, K. D., Tanelli, S., L'Ecuyer, T. S., Dzambo, A. M., Sy, O. O., McFarquhar, G. M., Poellot, M. R., Gupta, S., O'Brien, J. R., Nenes, A., Kacarab, M., Wong, J. P. S., Small-Griswold, J. D., Thornhill, K. L., Noone, D., Podolske, J. R., Schmidt, K. S., Pilewskie, P., Chen, H., Cochrane, S. P., Sedlacek, A. J., Lang, T. J., Stith, E., Segal-Rozenhaimer, M., Ferrare, R. A., Burton, S. P., Hostetler, C. A., Diner, D. J., Seidel, F. C., Platnick, S. E., Myers, J. S., Meyer, K. G., Spangenberg, D. A., Maring, H., and Gao, L.: An overview of the ORACLES (Observations of Aerosols above CLouds and their interactions) project: aerosol–cloud–radiation interactions in the southeast Atlantic basin, *Atmos. Chem. Phys.*, 21, 1507–1563, <https://doi.org/10.5194/acp-21-1507-2021>, 2021.
- Rogers, R. R., Hair, J. W., Hostetler, C. A., Ferrare, R. A., Obland, M. D., Cook, A. L., Harper, D. B., Burton, S. P., Shinozuka, Y., McNaughton, C. S., Clarke, A. D., Redemann, J., Russell, P. B., Livingston, J. M., and Kleinman, L. I.: NASA LaRC airborne high spectral resolution lidar aerosol measurements during M-LAGRO: observations and validation, *Atmos. Chem. Phys.*, 9, 4811–4826, <https://doi.org/10.5194/acp-9-4811-2009>, 2009.
- Ryoo, J.-M., Pfister, L., Ueyama, R., Zuidema, P., Wood, R., Chang, I., and Redemann, J.: A meteorological overview of the ORACLES (Observations of Aerosols above CLouds and their interactions) campaign over the southeastern Atlantic during 2016–2018: Part 1 – Climatology, *Atmos. Chem. Phys.*, 21, 16689–16707, <https://doi.org/10.5194/acp-21-16689-2021>, 2021.
- Sakaeda, N., Wood, R., and Rasch, P. J.: Direct and semi-direct aerosol effects of southern African biomass burning aerosol, *J. Geophys. Res.-Atmos.*, 116, D12205, <https://doi.org/10.1029/2010JD015540>, 2011.
- Sawamura, P., Moore, R. H., Burton, S. P., Chemyakin, E., Müller, D., Kolgotin, A., Ferrare, R. A., Hostetler, C. A., Ziemba, L. D., Beyersdorf, A. J., and Anderson, B. E.: HSRL-2 aerosol optical measurements and microphysical retrievals vs. airborne in situ measurements during DISCOVER-AQ 2013: an intercomparison study, *Atmos. Chem. Phys.*, 17, 7229–7243, <https://doi.org/10.5194/acp-17-7229-2017>, 2017.
- Schmid, B., Ferrare, R. A., Flynn, C., Elleman, R., Covert, D., Strawa, A., Welton, E., Turner, D., Jonsson, H., Redemann, J., Eilers, J., Ricci, K., Hallar, A. G., Clayton, M., Michalsky, J., Smirnov, A., Holben, B., and Barnard, J.: How well do state-of-the-art techniques measuring the vertical profile of tropospheric aerosol extinction compare?, *J. Geophys. Res.*, 111, D05S07, <https://doi.org/10.1029/2005JD005837>, 2006.
- She, C. Y., Alvarez II, R. J., Caldwell, L. M., and Krueger, D. A.: High-spectral-resolution Rayleigh-Mie lidar measurement of aerosol and atmospheric profiles, *Opt. Lett.*, 17, 541–543, 1992.
- Shingler, T., Crosbie, E., Ortega, A., Shiraiwa, M., Zuend, A., Beyersdorf, A., Ziemba, L., Anderson, B., Thornhill, L., Perring, A. E., Schwarz, J. P., Campazano-Jost, P., Day, D. A., Jimenez, J. L., Hair, J. W., Mikoviny, T., Wisthaler, A., and Sorooshian, A.: Airborne characterization of subsaturated aerosol hygroscopicity and dry refractive index from the surface to 6.5 km during the SEAC<sup>4</sup>RS campaign, *J. Geophys. Res.*, 121, 4188–4210, <https://doi.org/10.1002/2015JD024498>, 2016.
- Shinozuka, Y., Saide, P. E., Ferrada, G. A., Burton, S. P., Ferrare, R., Doherty, S. J., Gordon, H., Longo, K., Mallet, M., Feng, Y., Wang, Q., Cheng, Y., Dobracki, A., Freitag, S., Howell, S. G., LeBlanc, S., Flynn, C., Segal-Rozenhaimer, M., Pistone, K., Podolske, J. R., Stith, E. J., Bennett, J. R., Carmichael, G. R., da Silva, A., Govindaraju, R., Leung, R., Zhang, Y., Pfister, L., Ryoo, J.-M., Redemann, J., Wood, R., and Zuidema, P.: Modeling the smoky troposphere of the southeast Atlantic: a comparison to ORACLES airborne observations from September of 2016, *Atmos. Chem. Phys.*, 20, 11491–11526, <https://doi.org/10.5194/acp-20-11491-2020>, 2020.
- Shipley, S. T., Tracy, D. H., Eloranta, E. W., Tauger, J. T., Stroga, J. T., Roesler, F. L., and Weinman, J. A.: High spectral resolution lidar to measure optical scattering properties of atmospheric aerosols. 1. Theory and instrumentation, *Appl. Optics*, 22, 3716–3724, 1983.
- Stein, A. F., Draxler, R. R., Rolph, G. D., Stunder, B. J. B., Cohen, M. D., and Ngan, F.: NOAA's HYSPLIT atmospheric transport and dispersion modeling system, *B. Am. Meteorol. Soc.*, 96, 2059–2077, <https://doi.org/10.1175/BAMS-D-14-00110.1>, 2015.
- Veselovskii, I., Kolgotin, A., Grazianov, V., Müller, D., Wandinger, U., and Whiteman, D. N.: Inversion with regularization for the retrieval of tropospheric aerosol parameters from multi-wavelength lidar sounding, *Appl. Optics*, 41, 3685–3699, 2002.
- Wilcox, E. M.: Stratocumulus cloud thickening beneath layers of absorbing smoke aerosol, *Atmos. Chem. Phys.*, 10, 11769–11777, <https://doi.org/10.5194/acp-10-11769-2010>, 2010.
- Wilcox, E. M.: Direct and semi-direct radiative forcing of smoke aerosols over clouds, *Atmos. Chem. Phys.*, 12, 139–149, <https://doi.org/10.5194/acp-12-139-2012>, 2012.

- Wu, H., Taylor, J. W., Szpek, K., Langridge, J. M., Williams, P. I., Flynn, M., Allan, J. D., Abel, S. J., Pitt, J., Cotterell, M. I., Fox, C., Davies, N. W., Haywood, J., and Coe, H.: Vertical variability of the properties of highly aged biomass burning aerosol transported over the southeast Atlantic during CLARIFY-2017, *Atmos. Chem. Phys.*, 20, 12697–12719, <https://doi.org/10.5194/acp-20-12697-2020>, 2020.
- Xu, F., Gao, L., Redemann, J., Flynn C. J., Espinosa, W. R., da Silva, A. M., Starnes, S., Burton, S. P., Liu, X., Ferrare, R., Cairns, B., and Dubovik, O.: A Combined Lidar-Polarimeter Inversion Approach for Aerosol Remote Sensing Over Ocean, *Front. Remote Sens.*, 2, 620871, <https://doi.org/10.3389/frsen.2021.620871>, 2021.
- Yamaguchi, T., Feingold, G., Kazil, J., and McComiskey, A.: Stratocumulus to cumulus transition in the presence of elevated smoke layers, *Geophys. Res. Lett.*, 42, 10478–10485, 2015.
- Zhang, J. and Zuidema, P.: The diurnal cycle of the smoky marine boundary layer observed during August in the remote southeast Atlantic, *Atmos. Chem. Phys.*, 19, 14493–14516, <https://doi.org/10.5194/acp-19-14493-2019>, 2019.
- Zhang, X., Mao, M., Yin, Y., and Tang, S.: The absorption Ångstrom exponent of black carbon with brown coatings: effects of aerosol microphysics and parameterization, *Atmos. Chem. Phys.*, 20, 9701–9711, <https://doi.org/10.5194/acp-20-9701-2020>, 2020.
- Zhang, Z., Meyer, K., Yu, H., Platnick, S., Colarco, P., Liu, Z., and Oreopoulos, L.: Shortwave direct radiative effects of above-cloud aerosols over global oceans derived from 8 years of CALIOP and MODIS observations, *Atmos. Chem. Phys.*, 16, 2877–2900, <https://doi.org/10.5194/acp-16-2877-2016>, 2016.
- Zuidema, P., Redemann, J., Haywood, J., Wood, R., Piketh, S., Hipondoka, M., and Formenti, P.: Smoke and clouds above the southeast Atlantic, *B. Am. Meteorol. Soc.*, 97, 1131–1135, <https://doi.org/10.1175/BAMS-D-15-00082.1>, 2016.
- Zuidema, P., Sedlacek III, A. J., Flynn, C., Springston, S., Delgado, R., Zhang, J., Aiken, A. C., Koontz, A., and Muradyan, P.: The Ascension Island boundary layer in the remote Southeast Atlantic is often smoky, *Geophys. Res. Lett.*, 45, 4456–4465, <https://doi.org/10.1002/2017GL076926>, 2018.